crystals

MDPI

Article

Ferroelectric, Magnetic and Dielectric Properties of $SrCo_{0.2}Zn_{0.2}Fe_{11.6}O_{18.8}$ Hexaferrite Obtained by "One-Pot" Green Sol-Gel Synthesis Utilizing *Citrus reticulata* Peel Extract

Maria Vesna Nikolic [1,*], Souad Ammar-Merah [2], Nikola Ilić [3], Charanjeet Singh [4], Milena P. Dojcinovic [1] and Rajshree B. Jotania [5]

[1] Institute for Multidisciplinary Research, University of Belgrade, 11030 Belgrade, Serbia; milena.dojcinovic@imsi.bg.ac.rs
[2] ITODYS Laboratory, Université Paris Cité, CNRS UMR-7086, 75013 Paris, France; souad.ammar-merah@u-paris.fr
[3] Vinca Institute of Nuclear Sciences—National Institute of the Republic of Serbia, University of Belgrade, 11351 Belgrade, Serbia; nikola.ilic@vin.bg.ac.rs
[4] School of Electronics and Electrical Engineering, Lovely Professional University, Jalandar-Delhi, Phagwara 144001, Punjab, India; rcharanjeet@gmail.com
[5] Department of Physics, Electronics, and Space Science, School of Sciences, Gujarat University, Navrangpuram, Ahmedabad 380009, Gujarat, India; rbjotania@gmail.com
* Correspondence: mariavesna@imsi.bg.ac.rs

Abstract: $SrCo_{0.2}Zn_{0.2}Fe_{11.6}O_{18.8}$ hexaferrite was obtained by a "one-pot" green sol-gel synthesis method utilizing aqueous mandarin orange (*Citrus reticulata*) peel extract as an eco-friendly reactant. The research objective was to analyze the influence of cobalt and zinc co-doping and the synthesis process on the structure, morphology, magnetic, dielectric and ferroelectric properties of strontium hexaferrite in view of future applications. Structural and morphological characterization using X-ray diffraction (XRD), Fourier transform infrared spectroscopy (FTIR), and scanning electron microscopy coupled to energy dispersive X-ray spectrometry (SEM-EDX) confirmed the formation of a Co and Zn ion incorporated M-type magnetoplumbite with c/a lattice parameter ratio of 3.919 as crystallite nanoplatelets of 32 and 53 nm in thickness and width, respectively. The magnetic hysteresis loop of the synthesized powder recorded by a vibrating sample magnetometer (VSM) at room temperature confirmed its ferromagnetic nature with a coercive field (H_c) of 2539 Oe and a saturation magnetization (M_s) and remanent magnetization (M_r) of 44.6 emu/g and 21.4 emu/g, respectively. Room temperature ferroelectric loops measured at 100 Hz showed a maximal (P_{max}) and a remanent (P_r) polarization of 195.4 and 31.0 nC/cm^2, respectively. Both increased when the magnitude of the applied electrical field increased in the 1–24 kV/cm range. The dielectric constant decreased with the frequency increase, in accordance with the Maxwell–Wagner model, while the conductivity changed according to the Jonscher power law. The complex impedance was modeled with an equivalent circuit, enabling identification of the dominant contribution of grain boundary resistance (272.3 MΩ) and capacitance (7.16 pF).

Keywords: strontium hexaferrite; nanoplatelet; ferromagnetism; spontaneous polarization; ferroelectric properties; dielectric properties; complex impedance; green "one-pot" synthesis

Citation: Nikolic, M.V.; Ammar-Merah, S.; Ilić, N.; Singh, C.; Dojcinovic, M.P.; Jotania, R.B. Ferroelectric, Magnetic and Dielectric Properties of $SrCo_{0.2}Zn_{0.2}Fe_{11.6}O_{18.8}$ Hexaferrite Obtained by "One-Pot" Green Sol-Gel Synthesis Utilizing *Citrus reticulata* Peel Extract. *Crystals* **2023**, *13*, 1452. https://doi.org/10.3390/cryst13101452

Academic Editors: Floriana Craciun, Maria Dinescu and Mirjana Vijatovic Petrovic

Received: 5 September 2023
Revised: 22 September 2023
Accepted: 27 September 2023
Published: 29 September 2023

1. Introduction

Large amounts of fruit and vegetable peel are generated by the food industry and consumers. One way of utilizing such waste products is to use them as sources of eco-friendly reactants [1]. Green synthesis uses plant extracts for environmentally friendly synthesis of functional inorganic nanoparticles (NPs), and particularly metal oxide NPs. Thus, green root extract was used as a reducing and complexing pH stabilizer and/or dispersing agent to obtain X-type barium hexaferrite [2]. These extracts can be obtained

from different plants or plant waste, such as peel that contains alkaloids, amino acids, polysaccharides, tannins or other compounds that act as valuable reactants in the synthesis process, limiting the need for more toxic components. The resulting NPs have been shown to have improved antioxidant and antimicrobial properties [3,4]. They are also more biocompatible [5]. Thus, Amiri et al. [6] observed that nickel ferrite NPs obtained by green synthesis utilizing Urtica when exposed to a frequency magnetic field could cause cell death in human primary glioblastoma and neuroblastoma cancer cell lines. Zamani et al. [7] used hyaluronic acid-coated spinel ferrite NPs as part of an anticancer nanoplatform for combined phototherapy and chemotherapy for breast cancer treatment.

Citrus peel is seen as a good source of pectin and natural antioxidants, such as phenolic compounds, flavonoids or vitamin C [8,9]. Aqueous citrus extracts and also pectin citrus extracts have been successfully used as precursors in sol-gel synthesis of metal oxide NPs [10], including magnetic ones, like cobalt nanoferrites [8,11]. The sol-gel synthesis process is a simple, low-cost nanomaterial processing method, and when a citrus peel extract is used, it becomes more environmentally friendly.

M-type strontium hexaferrite $SrFe_{12}O_{19}$ is a hard magnetic material with a magnetoplumbite crystalline structure created by closely packed layers of Sr, Fe and O ions [12]. In this structure, the crystal lattice is formed of S (Fe_6O_8) and R ($SrFe_6O_{11}$) blocks following a set pattern (SRS*R*, with* denoting 180° rotation around the c-axis). It has been the subject of much research as a magnetic material due to its low cost, chemical stability, corrosion resistance and relatively high coercivity, remanence, saturation magnetization, electrical resistivity and low dielectric loss [13]. The synthesis method has a significant influence on resulting particle morphology, size and microstructure; thus, strontium hexaferrite has been synthesized using various methods, such as solid-state synthesis [14,15] and sol-gel [13,16] with calcination performed in the range 800–1100 °C.

In the $P6_3/mmc$ crystalline lattice, the iron Fe^{3+} ions can be located at five different crystallographic sites: octahedral (2*a*, 12*k* and $4f_2$), tetrahedral ($4f_1$) and trigonal bipyramid site (2*b*). The spin directions of Fe^{3+} ions on 12*k*, 2*a* and 2*b* sites are upward, and they are downward on $4f_1$ and $4f_2$ sites [15]. Thus, the magnetic structure can be described as ferrimagnetic with three parallel and two anti-parallel sublattices coupled by super-exchange interactions through the O^{2-} ions [16]. One widely investigated way to tune and change the magnetic properties of M-type strontium hexaferrite has been to partially replace Fe or Sr ions with other metal ions. Thus, among others, Sr has been partially replaced with Zr [17] or La [16], while Fe has been partially replaced by Cu [18] or Co [19]. Co-doping (double substitution) has also been the subject of much research, as the introduction of different combinations of magnetic and/or non-magnetic metal ions can have significant influences on the whole magnetic properties [12,20,21]. M-type strontium hexaferrite has been co-doped with Co-Ti [20], La-Zn [22], Co-Zr [21,23], Ni-Zr [21], La-Co [24], etc. Co-doping with a combination of one magnetic and one non-magnetic ion, such as, for example, Co-Zr or Ni-Zr, has been investigated with the purpose of reducing the large uniaxial crystalline anisotropy of M-type strontium hexaferrite [21]. Though both cobalt and zinc have been used as single dopants and/or co-dopants for M-type hexaferrites [19–24], to our knowledge, they have not been combined together as co-dopants for M-type hexaferrites. Mahmood et al. [25] investigated the influence of cobalt and zinc co-doping on structural and magnetic properties of Y-type hexaferrites, determining that zinc doping resulted in a reduction of the super-exchange coupling between various sublattices leading to a decrease in hyperfine magnetic fields.

Non-magnetic zinc (Zn^{2+}) ions introduced into M-type strontium hexaferrite have shown a preference for the spin-down $4f_1$ site, leading to an increased number of Fe^{3+} ions in spin-up sites and causing a small increase of the saturation magnetization (M_s) in low substitution ratio [22]. Magnetic cobalt (Co^{2+}) ions introduced into M-type strontium hexaferrite have shown a preference for tetrahedral $4f_1$ sites because a large Co^{2+} ionic radius of 0.58 Å can stabilize the S-block compared to 0.49 Å Fe^{3+} radius. However, the presence of even larger Fe^{2+} ions moves some Co^{2+} ions into octahedral sites [20]. Co^{2+}

ions split into trigonal bipyramidal 2*b* sites as well, and Co^{2+} ions in $4f_1$ and 2*b* sites have magnetic spins opposite to those of Fe^{3+} ions in octahedral positions, influencing magnetic properties in a complex way [20].

Strontium hexaferrite has been investigated and applied as a high-performance permanent magnetic material [22]. Recent focus has been on application as a suitable material for microwave absorption [18] or as a magnetoelectric multiferroic material [20]. Each type of application requires tuning of magnetic properties that are achieved most often by doping, co-doping and selecting or adjusting the synthesis process [21].

In this work, we have performed "one-pot" sol-gel synthesis of strontium hexaferrite, partially replacing iron with Co and Zn in order to obtain $SrCo_{0.2}Zn_{0.2}Fe_{11.6}O_{18.8}$ and utilizing mandarin orange (*Citrus reticulata*) peel extract as a complexing and dispersive agent in the synthesis process. We have performed a detailed analysis of the structure, morphology, magnetic, ferroelectric, dielectric and electrical properties in view of the dopant influence and application potential.

2. Materials and Methods

2.1. Powder Synthesis

Mandarin orange (*Citrus reticulata*) peel residue was collected from fruit purchased from the local market. A total of 550 g of this residue was mixed with 2.5 L of water, boiled for 30 min, cooled to room temperature and filtered through filter paper to obtain an aqueous extract. This extract contains natural antioxidant components that have been applied as reducing and stabilizing agents for sol-gel synthesis of oxide NPs [10]. The extract was stored in a fridge for further use. In order to synthesize co-doped strontium hexaferrite ($SrCo_{0.2}Zn_{0.2}Fe_{11.6}O_{18.8}$), the nitrate precursors were mixed in the calculated stoichiometric ratio. Typically, 0.9943 g of anhydrous strontium nitrate ($Sr(NO_3)_2$, ACS reagent, Roth, Karlsruhe, Germany), 22.01784 g of iron (III) nitrate nonahydrate ($Fe(NO_3)_3{\cdot}9H_2O$, ACS reagent, Sigma Aldrich, Merck KGaA, Darmstadt, Germany), 0.2735 g cobalt nitrate hexahydrate $Co(NO_3)_2{\cdot}6H_2O$ (Sigma Aldrich, puriss, p. a., Merck KGaA, Darmstadt, Germany) and 0.2795 g zinc nitrate hexahydrate ($Zn(NO_3)_2{\cdot}6H_2O$, reagent grade, Sigma Aldrich, Merck KGaA, Darmstadt, Germany) were mixed in 100 mL distilled water and 100 mL of the extract. The solution pH was set to 7 by adding 20 mL of ammonium hydroxide solution (28–30% ACS reagent, Sigma Aldrich, Merck KGaA, Darmstadt, Germany) and mixed at 90 °C on a magnetic mixer until a gel was formed. After increasing the temperature to 300 °C, gel combustion occurred, resulting in a black powder. Calcination was performed in a chamber furnace in two steps: the first at 500 °C for 3 h to remove any organic residue and the second at 950 °C for 6 h to crystallize the hexaferrite phase.

2.2. Characterization

In order to study the structural properties of the obtained powder, X-ray diffraction (XRD) data were collected on a PANalyticalX'Pert PRO diffractometer (Malvern Panalytical Ltd., Malvern, UK), operating within the Bragg–Brentano geometry for a scattering angle ranging between 10 and 120° (step 0.017 s, hold time 24.76 s) and equipped with a CoK_αX-ray tube. Fourier transform infrared (FTIR) spectra were measured (resolution—4 cm^{-1}, range 400–4000 cm^{-1}) on a FTIR Nicolet 6700 ATR device (Thermo Fisher Scientific, Waltham, MA, USA). Field emission scanning electron microscopy (FEG-SEM) coupled with energy dispersive X-ray spectrometry (EDX) analysis was applied to analyze the powder morphology on a ZEISS Gemini SEM 360 microscope (Zeiss Group, Oberkochen, Germany) on which an Oxford Instruments EDX spectrometer (Oxford Instruments, Abingdon, UK) is mounted.

In order to evaluate magnetic properties of the synthesized powder, magnetic characterization was conducted at room temperature on a vibrating sample magnetometer (Microsense EASY VSM 20180911-02, East Lowell, MA, USA) in the applied field range −15 to 15 kOe, with the measuring point density varying depending on the applied field

(±15 to 10 kOe, step size/sweep rate 1000 Oe, ±10 to 2.5 kOe step size/sweep rate 500 Oe, ±2.5 to 10 kOe, step size/sweep rate 200 Oe and ±1kOe to 0 step size/sweep rate 100 Oe).

Samples for ferroelectric and electric characterization were prepared by pressing 0.2 g of the synthesized powder mixed with several drops of a PVA solution under 2 tons into a disc pellet 8 mm in diameter. The prepared tablets were heated at 200 °C for 2 h (heating rate 10°/min). The resulting disc pellet density was determined as 2.351 g/cm^3. Ferroelectric properties were also measured on a Radiant Precision Multiferroic analyzer (Radiant Technologies, Inc., Albuquerque, NM, USA) aat room temperature (25 °C), with the applied voltage increasing up to 24 kV/cm until breakdown, single bipolar mode, hysteresis period 10 ms. The maximal applied voltage was calculated as 24 kV/cm as it depends on the sample surface and thickness, set by the instrument's limitation for maximal application voltage of 4 kV. Complex impedance was measured at room temperature on a HIOKI LCR 3536 analyzer (Hioki, Nagano, Japan) in the 50 Hz–1 MHz frequency range and enabled analysis of dielectric properties and complex impedance.

3. Results and Discussion

3.1. Phase Analysis

Analysis of the measured powder X-ray diffractogram with the help of HighScorePlus software indicated that a crystalline M-type hexaferrite phase (ICSD 98-006-9022) with a small secondary hematite phase (ICSD 98-017-4468, crystalline lattice rhombohedral) form the produced powder, as shown in Figure 1. The composition was estimated to be 90.6 wt.% of hexaferrite and 9.4 wt.% of hematite. Single-phase formation of M-type strontium hexaferrite depends on the synthesis procedure and parameters, including the calcination temperature, where a lower calcination temperature gives smaller particles as grain growth is limited, but secondary phases, often including hematite (α-Fe_2O_3), have been found [13,26]. The amount and type of substituting ion also have an influence, with secondary phases forming [26,27]. Thus, Bercoff et al. [26] analyzed the influence of Nd-Co substitution in $Sr(Nd, Co)_xFe_{12-x}O_{19}$, and for x = 0.4, they noted the formation of other iron oxides besides 60% of the hexagonal phase. Herme et al. [28] noted the formation of cubic spinel $CoFe_2O_4$ besides $NdFeO_3$ and Fe_2O_3 in sol-gel combustion synthesized M-type strontium hexaferrite.

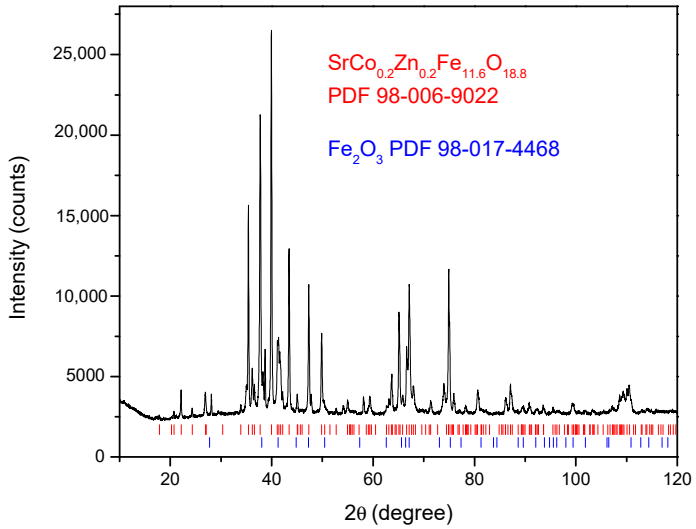

Figure 1. XRD pattern of the synthesized powder.

The d-lattice spacing in an M-type hexagonal crystalline structure can be calculated in the following way [29]:

$$\frac{1}{d_{hkl}^2} = \frac{4}{3}\left(\frac{h^2 + hk + k^2}{a^2}\right) + \frac{l^2}{c^2} \quad (1)$$

where d_{hkl}—is the interplanar spacing, and h, k and l are the Miller indices. Using this equation, the following lattice parameters were determined: a = 5.8832 Å and c = 23.0562 Å with c/a = 3.919. The c/a ratio is commonly used to confirm the M-type structure ($P6_3/mmc$ crystalline lattice) when below 3.98 [12,19], as is the case here. The determined lattice constant values were in line with values obtained for co-doped M-type strontium hexaferrites [12]. The crystallite size was determined using the Scherrer equation. In the case of hexaferrites, due to the formation of typical hexagonal platelets, the crystallite size is often determined along two directions [30]. The first is along the [00*l*] axis, which describes the platelet thickness, while the second describes the crystallite width along the [*hk*0] axis. Focusing on the well-defined (008) and (110) hexaferrite diffraction lines, we found a crystallite platelet thickness of 32 nm and a width of 53 nm.

To complete these structural characterizations, the ATR-FTIR spectrum of the obtained powder was recorded (Figure 2). According to group theoretical analysis, strontium hexaferrites have 13 A_{2u} + 18 E_{1u} active infrared modes [31]. In our spectrum, we noted three vibration bands at 583, 541 and 421 cm^{-1}. These vibration bands have been noted before for metal-oxygen vibrations in the hexaferrite structure [21,32]. Hematite also has vibration modes in this region; thus, Justus et al. [33] determined two bands originating from iron-oxygen vibrations, one stretching at 460 and one bending at 540 cm^{-1} in hematite. The presence of hematite cannot be confirmed using FTIR, as the bands overlap with the hexagonal structure. Complete burn-out of all the nitrate precursors and the citrus peel extract can also be confirmed as no noticeable vibration bands are present above the metal-oxygen vibrations.

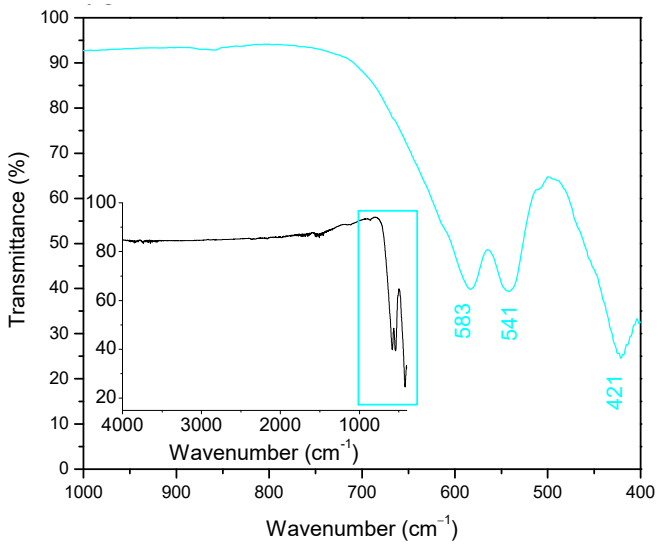

Figure 2. FTIR spectrum of the synthesized powder, the black line represents the whole measured range, while the blue line represents the range 1000-400 cm.

3.2. Microstructural Analysis

The microstructure of the synthesized powder was mainly investigated by SEM observations. The collected micrographs are given in Figure 3. They are typical of hexagonal structures. The powder consisted of randomly oriented and aggregated hexagonal nanoplatelets, as noted before for this material [21]. EDX analysis performed on a number of areas confirmed the presence of Co, Zn, Sr, Fe, and O in atomic and weight percentages close to the expected $SrCo_{0.2}Zn_{0.2}Fe_{11.6}O_{18.8}$ stoichiometry, namely $Sr_{1.0}Co_{0.37}Zn_{0.30}Fe_{12.98}O_{20.19}$. Slightly larger amounts of oxygen and iron can also be the consequence of EDX analysis, taking into account the surface of the material and selected areas, including more than one particle and also relating to the presence of hematite. Such relatively small deviations have been observed before for doped strontium hexaferrite [21,34,35], with EDX showing basic

agreement between calculated and observed values. The distribution of Co and Zn ions was homogenous within the hexaferrite structure [36].

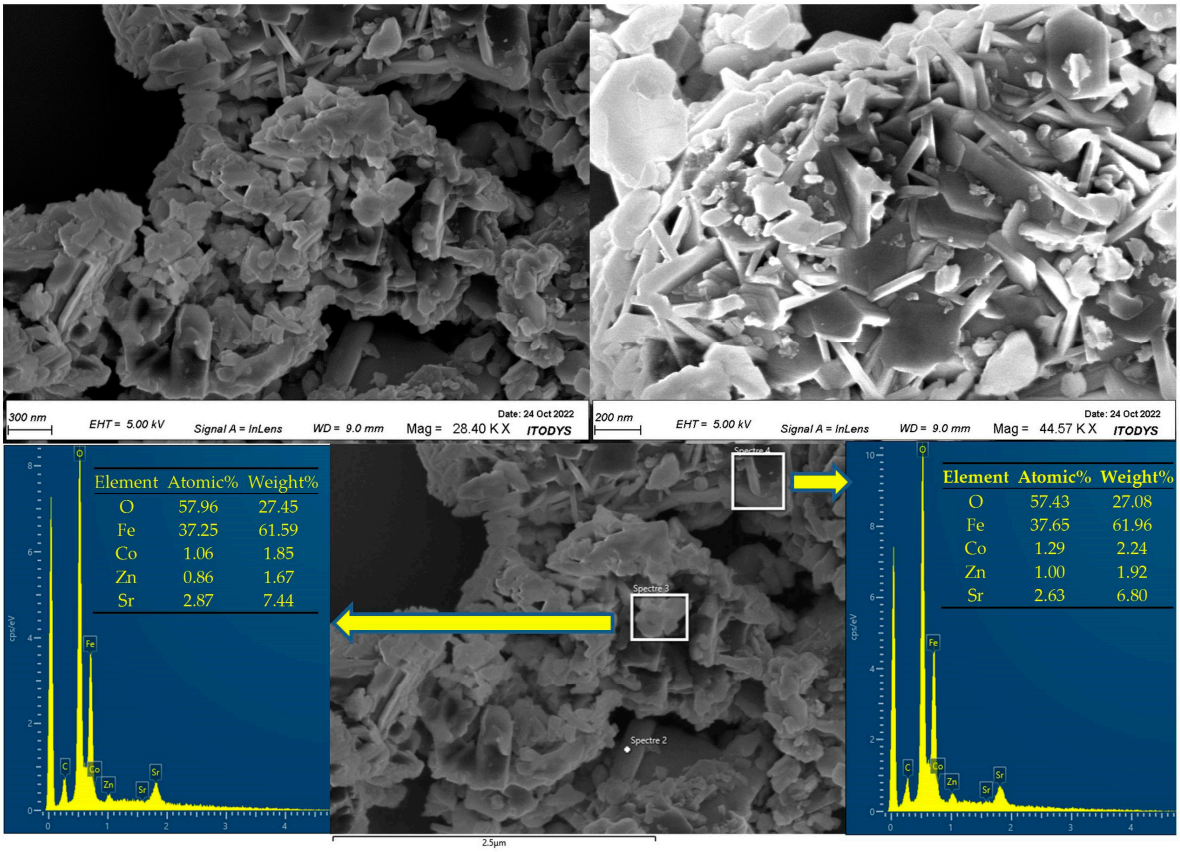

Figure 3. SEM micrographs of the synthesized powder, selected areas for EDX analysis and tables with quantitative elemental analysis confirming the $SrCo_{0.2}Zn_{0.2}Fe_{11.6}O_{18.8}$ composition.

3.3. Magnetic Properties

The magnetic hysteresis loop measured for the synthesized powder is shown in Figure 4a. The hysteresis loop demonstrates non-linearity in the curve around the low applied magnetic field, as a kink can be seen in the loop. This has been noted before for hexaferrites and indicates the presence of other magnetic phases [37–39]. In this case the kink is attributed to weak exchange coupling between the M-phase of strontium hexaferrite and the hematite phase, as weak magnetic behavior is the characteristic feature of hematite, while M-type strontium ferrite has a hard magnetic nature [40,41]. A similar influence of hematite as a second/residual phase has been noted before [38,42].

A better insight into what is occurring inside the synthesized powder under a magnetic field can be achieved by differentiating the hysteresis loop and plotting the resulting dM/dH curves (Figure 4b). For a hard magnet, we expect a smooth broad hysteresis, and the differential curve should exhibit one single symmetrical broad peak at a certain value of H. In our case, we obtained two peaks: one sharp at $H \approx 0$ and one broad at $\mu_0 H \approx 0.55$ T (H = 5500 Oe). This is characteristic of weakly coupled magnetic systems and can be the result of structural factors [42] like the superposition of a soft and a hard magnet and hematite exhibiting weak ferromagnetism above its Morin transition temperature of 250 K. Için et al. [38] linked kink formation in the hysteresis loop with dopant substitution of iron in the hexaferrite lattice, where increased dopant (Cr^{3+}) amounts replacing iron in the strontium hexaferrite led to a more pronounced kink due to increased hematite formation. Choi et al. [39] associated the "kinks" as a discrepancy between the magnetic anisotropy field and the coercive field originating from the non-ideal motion of magnetic domains due to non-uniform magnetization reversal and heterogeneities in the sample microstructure.

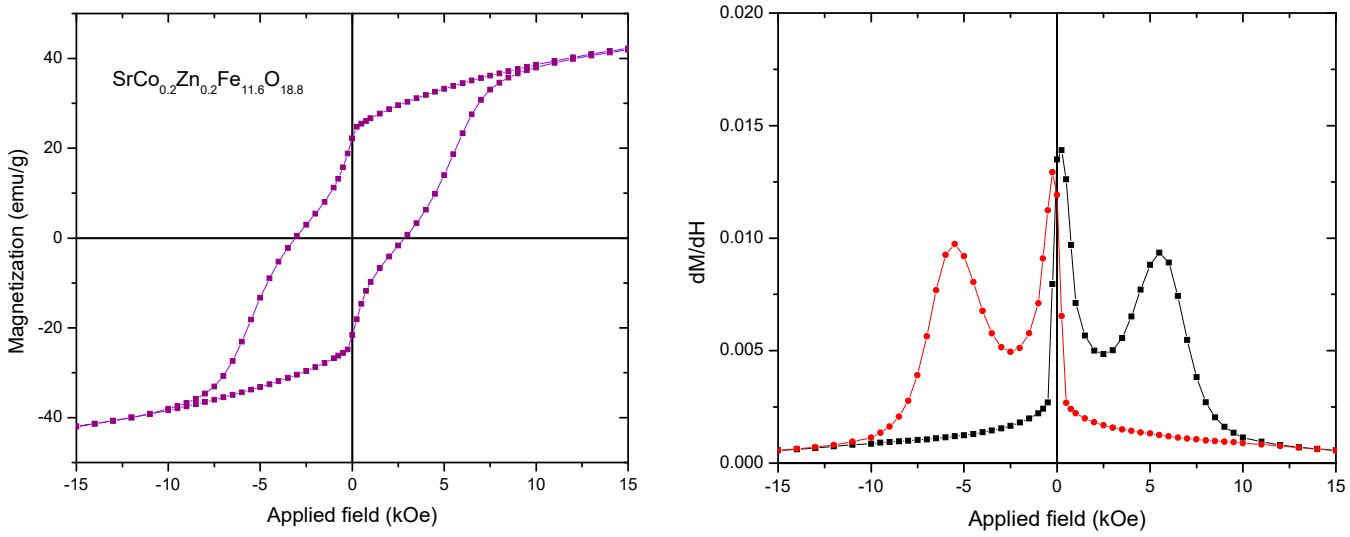

(**a**) (**b**)

Figure 4. (**a**) Magnetic hysteresis loop; (**b**) dM/dH—switching field distribution curves of the synthesized powder at room temperature (red and black represent trace and retrace parts of the hysteresis loop).

The coercive field (H_c) was determined as 2539 Oe, saturation magnetization (M_s) as 44.6 emu/g, remanent magnetization (M_r) as 21.4 emu/g, and with a squareness factor (M_r/M_s) of 0.48. These values are in the range previously determined for doped and co-doped strontium hexaferrite [21,43] and reflect the influence of co-doping with Co and Zn. They are lower than the values commonly measured for pure strontium hexaferrite [38,39]. They are very similar to the values obtained for indium-doped strontium hexaferrite—$SrFe_{10.8}In_{1.2}O_{19}$ [44].

According to the Stoner–Wohlfarth model, the M_r/M_s ratio of 0.5 is associated with randomly oriented non-interacted particles/crystallites with uniaxial polycrystalline anisotropy, implying a weak exchange interaction [45,46]. In our case, M_r/M_s is close to 0.5, which confirms the poor exchange interaction of the M-phase and the hematite phase. Furthermore, the same ratio value (0.5) is for single domain particles, which are difficult to magnetize and need a more applied field to magnetize; thus, low M_s is observed. It is noteworthy that the high slope in the MH loop at the maximum applied field is attributed to this single-domain nature as well as the shape anisotropy of platelet-type grains.

The magnetic properties depend on many factors that include morphology, grain size, chemical doping or contamination and/or crystallographic lattice site occupancy. These factors affect the $Fe^{3+}-O-Fe^{3+}$ exchange interactions [21]. In our case, we have introduced both a magnetic ion Co^{2+} and a non-magnetic (diamagnetic) ion Zn^{2+} to substitute part of Fe^{3+}. Magnetic cobalt ions with a magnetic moment of 3 μ_B (compared to 5 μ_B for Fe^{3+}) can lead to the weakening of super-exchange interactions between oxygen and iron ions. Cobalt with fewer unpaired electrons than Fe^{3+} can reside in spin-down $4f_1$ sites but also in the octahedral 12k site and the bipyramidal 2b site, having a varied influence on the magnetic properties [21]. Combined with the presence of zinc ions with a preference for the spin-down $4f_1$ site, this results in magnetic properties different from pure strontium hexaferrite.

The crystal size decrease in the nanometer scale also means uncoupled surface Fe^{3+}cations, with the magnetic interaction pathway being broken at the border of the hexaferrite particles. The spin canted nature of hematite (9.4 wt.%) also contributes to the decrease in the total magnetic moment of the produced powder since its magnetization is significantly smaller than that of strontium hexaferrite [27,40].

3.4. Ferroelectric Properties

The ferroelectric properties of the produced powder were mainly characterized by measuring the polarization p versus electrical field E hysteresis loops at room temperature. Increasing the applied electric field to 24 kV/cm led to a noticeable increase in the maximal polarization (P_{max}) and the remanent polarization (P_r), as shown in the $P(E)$ loops measured at 100 Hz (Figure 5a,b). Due to the inability to measure these samples in higher fields, the saturation polarization could not be determined. The loop is a typical unsaturated loop with very low polarization and a small ratio of remanent to maximal polarization. The coercive electric field is quite high, going up to 3500 V/cm for maximal achieved fields. It does not exhibit a leaky shape, so we can expect all of the mentioned values to be higher. The appearance of hysteresis loops and remanent polarization at room temperature confirms the ferroelectric behavior inferred from the hexaferrite phase. Ferroelectric properties of hexaferrites have been noted before and include both barium and strontium hexaferrites [47–49]. This characteristic of hexaferrites has been linked to specifics of their structure with unequal distortions of neighboring polyhedra and broken spatial inversion symmetry [44,49].

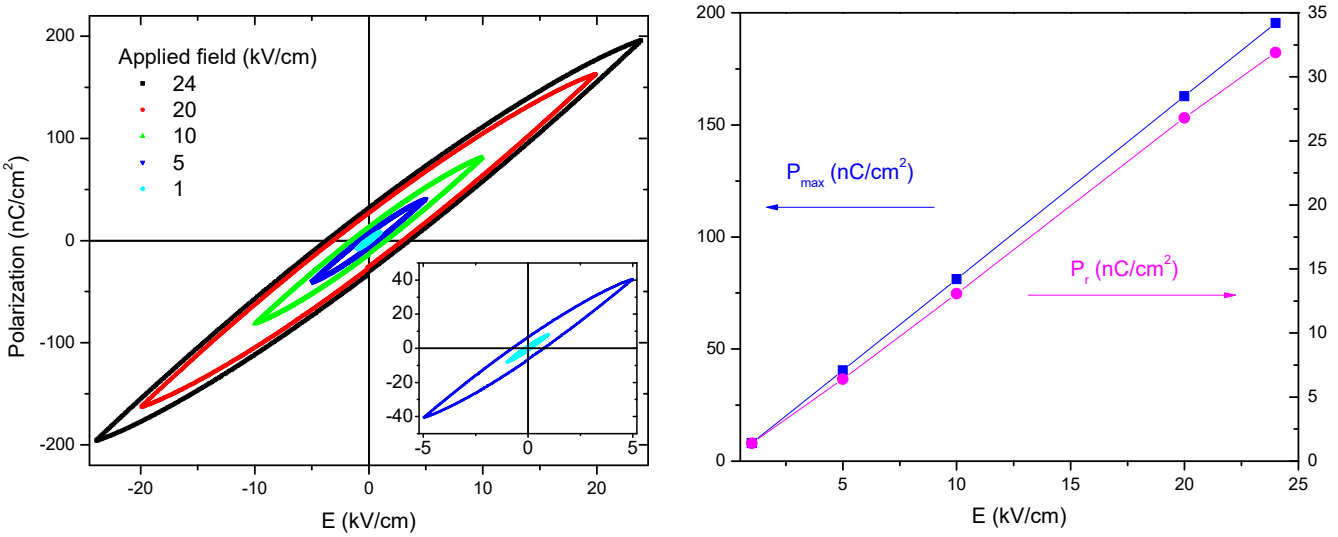

(**a**) (**b**)

Figure 5. (**a**) Ferroelectric hysteresis loops measured at 100 Hz on the produced powder; (**b**) Maximal and remanent polarization change with applied electric field in the range 1−24 kV/cm.

3.5. Dielectric Properties

The dielectric properties of the produced powder were examined by measuring their dielectric constant, their electrical conductivity and complex impedance at room temperature. The measured room temperature complex impedance, $Z = R + jX$, where R is the resistance and real part of the impedance and X is the reactance and its imaginary part, allowed the determination of $|Z| = \sqrt{R^2 + X^2}$, plotting it for different electrical field frequencies (Figure 6a). It decreases with increasing frequency in the measured frequency range. This $|Z|$ decrease is more noticeable in the lower frequency range. Small dissipation is noted in the range of 100–500 Hz, probably due to the high resistance values obtained.

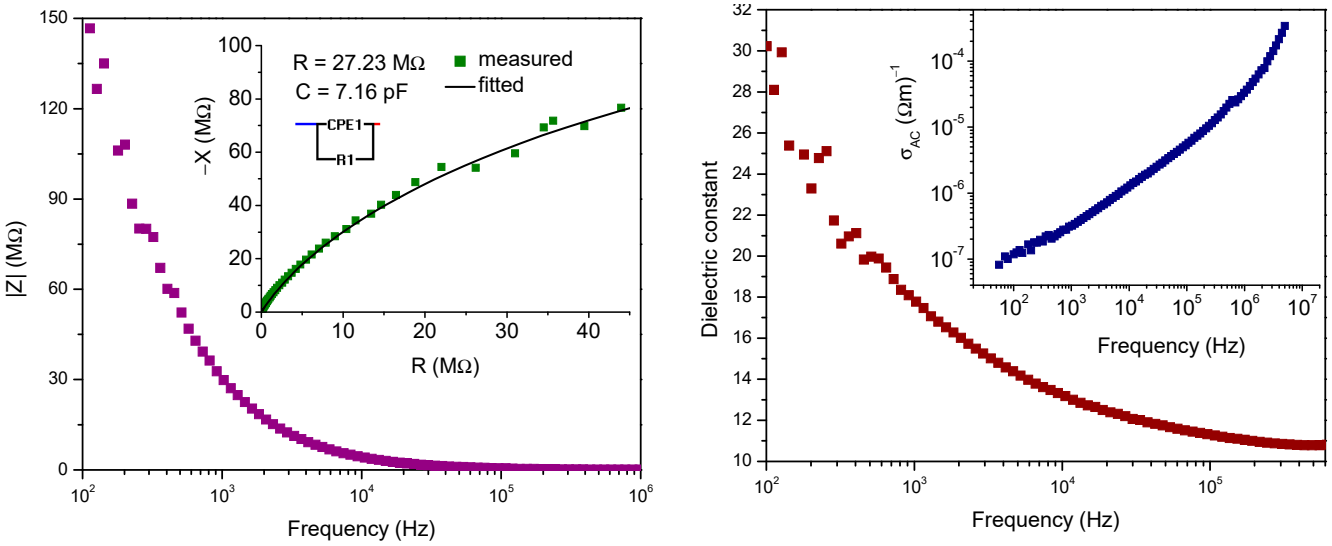

(**a**) (**b**)

Figure 6. (**a**) Complex impedance |Z| dependence on frequency. Inset: Complex impedance (Cole-cole) plot; points denote measured values while the line represents fitting with an equivalent circuit composed of parallel resistance and CPE element; (**b**) Dielectric constant dependence on frequency. Inset: AC conductivity dependence on frequency of the produced powder, as determined at room temperature.

The Cole–Cole plot of the real and imaginary components of the measured impedance is shown in the inset of Figure 6a. One partial semicircle can be noted, and this is in accordance with the previous analysis of M-type strontium hexaferrite performed by Bhat et al. [50]. The Cole–Cole plot of the measured impedance enables a better understanding of the contributions of grains and grain boundaries in the material and the interface effects on the electrical properties [50]. The semicircle appearing in the lowest frequency range is due to interface effects, while the grain boundary influence is in the intermediate frequency range, with the grain influence in the highest frequency range. One partial semicircle denotes a dominant influence of one relaxation mechanism. The absence of a noticeable semicircle in the high frequency range that is the result of grains, compared to the noticeable semicircle in the lower frequency range, indicates the dominant influence of grain boundaries [51]. The measured impedance was modeled using the EISA software [52], and an equivalent circuit consisting of a parallel resistance and constant phase element (CPE) commonly used instead of the capacitance component when non-ideal Debye behavior is observed [53]. This behavior is reflected as a depressed semicircle whose center lies below the axis, and in our case, n = 0.8684. The grain boundary resistance was determined as 272.3 MΩ, while the capacitance was determined from the calculated resistance and CPE parameter values ($A = 1.6292 \times 10^{-11}$ and n = 0.8684) using the equation given in [53] as 7.16 pF. The fitting error was below 2%, showing good agreement of the proposed equivalent circuit with the measured impedance. The relaxation time for grain boundaries was determined as 1.95×10^{-3} s.

The dielectric constant was calculated from the measured impedance as [53]:

$$\varepsilon\prime = \frac{X}{\omega C_0 Z^2} \quad (2)$$

where X is the imaginary part of the impedance, ω is the angular frequency, and C_0 is the capacitance of the corresponding air gap parallel plate capacitor with the same dimensions as the tested sample and is calculated as:

$$C_0 = \frac{d^2 \pi \varepsilon_0}{4h \cdot 1000} \quad (3)$$

where d is the sample diameter, h is the sample height, and ε_0 is the permittivity of free space.

The determined dielectric constant at room temperature, mainly due to the hexaferrite phase, is shown in Figure 6b. We can note that it decreases from around 30 at 100 Hz with increasing frequency, reaching the value of 10.5 at 1 MHz. This is similar to previous research on M-type strontium hexaferrites [50]. This type of behavior of the dielectric constant is in accordance with the Maxwell–Wagner type of interfacial polarization applied for heterogeneous systems [51,54]. In the lower frequency domain, the dielectric behavior is influenced by the heterogeneous system composed of grains and grain boundaries with different conducting properties [50]. Neglecting hematite contribution and taking into account the ferromagnetic and ferroelectric properties of $SrCo_{0.2}Zn_{0.2}Fe_{11.6}O_{18.8}$ hexaferrite determined and analyzed above, the different conductivity contributions of ferromagnetic and ferroelectric phases also participate in the interfacial polarization mechanism [55].

The AC conductivity was calculated as:

$$\sigma_{AC} = \frac{\varepsilon_0 \cdot R}{C_0 Z^2} \quad (4)$$

where R is the real part of the impedance, and the other parameters have been described above for Equations (2) and (3). The determined conductivity for $SrCo_{0.2}Zn_{0.2}Fe_{11.6}O_{18.8}$ hexaferrite is shown in the inset in Figure 6b. It changes according to the Jonscher power law, being relatively constant in the lower frequency range and increasing with frequency increase as [53,54]:

$$\sigma_{AC} = \sigma_{DC} + A\omega^s \quad (5)$$

where ω is the angular frequency, σ_{DC} is the frequency-independent and temperature-dependent component of conductivity, A is the pre-exponential factor, and s is the frequency exponent. In the logarithmic scale, the frequency exponent can be determined from the slope, and the determined value is 0.65. For determined $s < 1$, the conduction is due to the hopping of charge carriers, in this case, between Fe^{3+} ions [50].

4. Conclusions

Cobalt and zinc co-doped M-type magnetoplumbite strontium hexaferrite $SrCo_{0.2}Zn_{0.2}Fe_{11.6}O_{18.8}$ was obtained using one-pot green sol-gel synthesis utilizing nitrate precursors and mandarin orange peel extract and subsequent calcination at 950 °C. Analysis of the diffraction pattern confirmed the formation of M-type hexagonal strontium hexaferrite-90.6 wt.% with a hematite secondary phase of 9.4 wt.%. The crystallite size was determined using the Scherrer equation, using well-defined (008) and (110) diffraction lines, establishing nanoplatelets 32 nm thick and 53 nm wide. Analysis of the microstructure and morphology showed the homogenous distribution of cobalt and zinc in the powder and randomly oriented aggregated hexagonal nanoplatelets. Measurement of magnetic properties confirmed the ferromagnetic nature of the obtained powder, while measurement of the ferroelectric properties showed the ferroelectric nature of this powder at room temperature. The powder showed a high resistance at room temperature with a dominant influence of grain boundaries on the complex impedance. Future research will focus on further investigation of the application potential of this material in the microwave frequency range in a wide temperature range and for ultra-low power high-density data storage.

Author Contributions: Conceptualization: M.V.N., C.S. and R.B.J.; methodology: M.V.N.; investigation: M.V.N., S.A.-M., N.I. and M.P.D.; writing—original draft preparation: M.V.N., S.A.-M. and N.I.; writing—review and editing: M.V.N., S.A.-M., C.S., N.I., M.P.D. and R.B.J.; supervision: M.V.N. All authors have read and agreed to the published version of the manuscript.

Funding: This research was funded by the Ministry for Science, Technological Development and Innovations of the Republic of Serbia, contracts 451-03-47/2023-1/200053 (M.V.N. and M.P.D.), 451-03-47/2023-1/200017 (N.I.).

Data Availability Statement: The data presented in this study are available on request from the corresponding authors. The data are not publicly available due to ongoing research.

Acknowledgments: We are grateful to Sarra Gam-Derouich at ITODYS laboratory, Université Paris Cité for help with FEG-SEM and EDX measurements, and Smilja Markovic at the Institute of Technical Sciences of SASA for help with FTIR measurements.

Conflicts of Interest: The authors declare no conflict of interest. The funders had no role in the design of the study; in the collection, analyses, or interpretation of data; in the writing of the manuscript; or in the decision to publish the results.

References

1. Kumar, H.; Bhardwaj, K.; Sharma, R.; Nepovimova, E.; Kuca, K.; Dhanjal, D.S.; Verma, R.; Bhardwaj, P.; Shrama, S.; Kumar, D. Fruit and vegetable peels: Utilization of high value horticultural waste in novel industrial applications. *Molecules* **2020**, *5*, 2812. [CrossRef] [PubMed]
2. Kagdi, A.; Pullar, R.C.; Meena, S.S.; Jotania, R.B.; Batoo, K.M. Studies of structural, magnetic and dielectric properties of X-type barium zinc hexaferrite $Ba_2Zn_2Fe_{28}O_{46}$ powder prepared by combustion treatment method using ginger root extract as a green reducing agent. *J. Alloys Compd.* **2020**, *842*, 155120. [CrossRef]
3. Gao, Y.; Xu, D.; Ren, D.; Zeng, K.; Wu, X. Green synthesis of zinc oxide nanoparticles using Citrus sinensis peel extract and application to strawberry preservation: A comparison study. *LWT Food Sci. Technol.* **2020**, *126*, 109297. [CrossRef]
4. Hamarawf, R.F.; Tofiq, D.I.; Omer, K.M. Green synthesis of M-type manganese-substituted strontium hexaferrite $SrMn_xFe_{12-x}O_{19}$ nanoparticles with intrinsic antibacterial activity against human pathogenic bacteria. *New J. Chem.* **2023**, *47*, 15236–15249. [CrossRef]
5. Narayanam, K.B.; Sakhtivel, N. Green synthesis of biogenic metal nanoparticles by terrestrial and aquatic phototrophic and heterotrophic eukaryotes and biocompatible agents. *Adv. Colloid Interface Sci.* **2011**, *169*, 59–79. [CrossRef]
6. Amiri, M.; Pardakhti, A.; Ahmadi-Zeidabadi, M.; Akbari, A.; Salavati-Niasari, M. Magnetic nickel ferrite nanoparticles: Green synthesis of Urtica and therapeutic effect of frequency magnetic field on creating cytotoxic response in neural cell lines. *Colloids Surf. B* **2018**, *172*, 244–253. [CrossRef]
7. Zamani, M.; Aghajanzadeh, M.; Jashnani, S.; Shahangian, S.S.; Shirini, F. Hyaluronic acid coated spinel ferrite for combination of chemo and photodynamic therapy: Green synthesis, characterization in an in vitro and in vivo biocompatibility study. *Int. J. Biol. Macromol.* **2022**, *219*, 709–720. [CrossRef]
8. Proveti, J.R.C.; Porto, P.S.S.; Muniz, E.P.; Pereiro, R.D.; Araujo, D.R.; Solveira, M.B. Sol-gel proteic method using orange albedo pectin for obtaining cobalt ferrite particles. *J. Sol-Gel Sci. Tehnol.* **2015**, *75*, 31–37. [CrossRef]
9. Sir Elkhatim, K.A.; Elagib, R.A.A.; Hassan, A.B. Content of phenolic compounds and Vitamin C and antioxidant activity in wasted parts of Sudanese citrus fruit. *Food Sci. Nutr.* **2018**, *6*, 1214–1219. [CrossRef]
10. Thi, T.U.D.; Nguyen, T.T.; Thi, Y.D.; Thi, K.H.T.; Phan, B.T.; Pham, K.N. Green synthesis of ZnO nanoparticles using orange fruit peel extract for antibacterial activities. *RSC Adv.* **2020**, *10*, 23899–23907. [CrossRef]
11. Muniz, E.P.; de Assuncao, L.S.D.; de Souza, L.M.; Ribeiro, J.J.K.; Marqes, W.P.; Pereira, R.D.; Porto, P.S.S.; Proveti, J.R.C.; Passamani, E.C. On cobalt ferrite production by sol-gel from orange fruit residue by three related procedures and its application in oil removal. *J. Clean. Prod.* **2020**, *265*, 121712. [CrossRef]
12. Liu, C.; Kan, X.; Hu, F.; Liu, X.; Feng, S.; Wu, J.; Wang, W.; Rehman, U.; Shezad, M.; Zhang, C.; et al. Investigations of Ce-Zn co-substitution on crystal structure and ferromagnetic properties of M-type strontium hexaferrite $Sr_{1-x}Ce_xFe_{12-x}Zn_xO_{19}$ compounds. *J. Alloys Compd.* **2019**, *785*, 452–459. [CrossRef]
13. Alamolhoda, S.; Seyyed Ebrahimi, S.A.; Badiei, A. A study on the formation of strontium hexaferritenanopowder by a sol-gel auto-combustion method in the presence of a surfactant. *J. Magn. Magn. Mater.* **2006**, *303*, 69–72. [CrossRef]
14. Kiani, E.; Rozatian, A.S.; Yousefi, M.H. Synthesis and characterization of $SrFe_{12}O_{19}$ nanoparticles produced by a low temperature solid-state reaction method. *J. Mater. Sci. Mater. Electron.* **2013**, *24*, 2485–2492. [CrossRef]
15. Obradors, X.; Collomb, A.; Pernet, M.; Samaras, D.; Joubert, J.C. X-ray analysis of the structural and dynamic properties of $BaFe_{12}O_{19}$ hexagonal ferrite at room temperature. *J. Solid State Chem.* **1985**, *56*, 171–181. [CrossRef]
16. Dang, T.M.H.; Truh, V.D.; Bui, D.H.; Phan, M.H.; Huynh, D.C. Sol-gel hydrothermal synthesis of strontium hexaferrite nanoparticles and the relation between their crystal structure and high coercivity properties. *Adv. Nat. Sci. Nanosci. Nanotechnol.* **2012**, *3*, 025015. [CrossRef]

17. Almessiere, M.A.; Slimani, Y.; Sertkol, M.; Nawaz, M.; Baykal, A.; Ercan, I. The impact of Zr substituted Srhexaferrites investigation on structure, optic and magnetic properties. *Results Phys.* **2019**, *13*, 102244. [CrossRef]
18. Maramu, N.; Sriramulu, G.; Ramesh, T.; Ravinder, D.; Katlakunta, S.; Anil Babu, T.; Krishna Prasad, N.N. Crystal chemistry, Rietveld analysis, magnetic and microwave properties of Cu-doped strontium hexaferrites. *J. Mater. Sci. Mater. Electron.* **2021**, *32*, 10376–10387. [CrossRef]
19. Liu, X.S.; Fernandez-Garcia, L.; Hu, F.; Zhu, D.R.; Suarez, M.; Mendez, J.L. Magneto-optical Kerr spectra and magnetic properties of Co-substituted M-type strontium ferrites. *Mater. Chem. Phys.* **2012**, *133*, 961–964. [CrossRef]
20. Beevers, J.E.; Love, C.J.; Lazarov, V.K.; Cavill, S.A.; Izadkhah, H.; Vittoria, C.; Fan, R.; van der Laan, G.; Dhesi, S.S. Enhanced magnetoelectric effect in M-type hexaferrites by Co substitution into trigonal bi-pyramidal sites. *Appl. Phys. Lett.* **2018**, *112*, 082401. [CrossRef]
21. Almessiere, M.A.; Slimani, Y.; DemirKorkmaz, A.; Guner, S.; Maarouf, A.A.; Baykal, A. Comparative study of sonochemically synthesized Co-Zr and Ni-Zr substituted Sr-hexaferrites: Magnetic and structural investigations. *J. Magn. Magn. Mater.* **2020**, *497*, 165996. [CrossRef]
22. Bai, J.; Lu, X.; Xie, T.; Wei, F.; Yang, Z. The effects of La-Zn substitution on the magnetic properties of Sr-magnetoplumbic ferrite nanoparticles. *Mater. Sci. Eng. B* **2000**, *68*, 182–185. [CrossRef]
23. Kaur, P.; Chawla, S.K.; Meena, S.S.; Yusuf, S.M.; BindraNarang, S. Synthesis of Co-Zr doped nanocrystalline strontium hexaferrites by sol-gel auto-combustion route using sucrose as fuel and study of their structural, magnetic and electrical properties. *Ceram. Int.* **2016**, *42*, 14475–14489. [CrossRef]
24. Hwang, T.Y.; Lee, J.; Lim, H.R.; Jeong, S.J.; An, G.H.; Kim, J.; Choa, Y.H. Synthesis and magnetic properties of La^{3+}-Co^{2+} substituted strontium ferrite particles using modified spray pyrolysis-calcination method. *Ceram. Int.* **2017**, *43*, 3879–3884. [CrossRef]
25. Mahmood, S.H.; Jaradat, F.S.; Lehlooh, A.F.; Hammoudeh, A. Structural properties and hyperfine interactions in Co-Zn Y-type hexaferrites prepared by the sol-gel method. *Ceram. Int.* **2014**, *40*, 5231–5236. [CrossRef]
26. Bercoff, P.G.; Henue, C.; Jacobo, S.E. The influence of Nd-Co substitution on the magnetic properties of non-stoichiometric strontium hexaferrite nanoparticles. *J. Magn. Magn. Mater.* **2009**, *321*, 2245–2250. [CrossRef]
27. Ghezelbash, S.; Yousefi, M.; Hossainsadr, M.; Baghshahi, S. Structural and magnetic properties of Sn^{4+} doped strontium hexaferrites prepared via sol-gel auto-combustion method. *IEEE Trans. Magn.* **2018**, *54*, 2001306. [CrossRef]
28. Herme, C.A.; Bercoff, P.G.; Jacobo, S.E. Nd-Co substituted strontium hexaferrite powders with enhanced coercivity. *Mater. Res. Bull.* **2012**, *47*, 3881–3887. [CrossRef]
29. Klug, H.P.; Alexander, L.E. *X-ray Diffraction Procedures: For Polycrystalline and Amorphous Materials*, 2nd ed.; Wiley: Hoboken, NJ, USA, 1974; p. 992.
30. Shekhamat, D.; Roy, P.K. Effect of cobalt substitution on physical and electromagnetic properties of $SrAl_4Fe_8O_{19}$ hexaferrite. *Mater. Chem. Phys.* **2019**, *229*, 183–189. [CrossRef]
31. Nikolic, P.M.; Zivanov, L.; Aleksic, O.S.; Samaras, D.; Gledhill, G.A.; Collins, J.D. FIR optical properties of single crystal Ba- and Sr-hexaferrite. *Infrared Phys.* **1990**, *20*, 265–269. [CrossRef]
32. Maramu, N.; Ravinder, D.; Babu, T.A.; Reddy, B.R.; Srivamulu, G.; Sadhara, K.; Prasad, N.V.K. Structural and microwave properties of Ag-doped strontium hexaferrite. *J. Mater. Sci. Mater. Electron.* **2021**, *32*, 23854–23862. [CrossRef]
33. Justus, J.S.; Roy, S.D.D.; Raj, A.M.E. Synthesis and characterization of hematite nanopowders. *Mater. Res. Express* **2016**, *3*, 105037. [CrossRef]
34. Auwal, I.A.; Güngünes, H.; Baykal, A.; Guner, S.; Shirsath, S.E.; Sertkol, M. Structural, morphological, optical, cation distribution and Mössbauer analysis of Bi^{3+} substituted strontium hexaferrite. *Ceram. Int.* **2016**, *42*, 8627–8635. [CrossRef]
35. Iqbal, M.J.; Ashiq, M.N.; Gul, I.H. Physical, electrical and dielectric properties of Ca-substituted strontium hexaferrite ($SrFe_{12}O_{19}$) nanoparticles synthesized by co-precipitation method. *J. Magn. Magn. Mater.* **2010**, *322*, 1720–1726. [CrossRef]
36. Hu, C.; Cao, H.; Wang, S.; Wu, N.; Qiu, S.; Lyu, H.; Liu, J. Synthesis of strontium hexaferritenanoplates and the enhancement of their electrochemical performance by Zn^{2+} doping for high-rate and long-life lithium ion batteries. *New J. Chem.* **2017**, *41*, 6427–6435. [CrossRef]
37. Manglam, M.K.; Mallick, J.; Kumari, S.; Pandey, R.; Kar, M. Crystal structure and magnetic properties study on barium hexaferrite (BHF) and cobalt zinc ferrite (CZF) in composites. *Solid State Sci.* **2021**, *113*, 106529. [CrossRef]
38. Için, S.; Öztürk, S.; Çakil, D.D.; Sünbül, S.E.; Ergin, I.; Özçelik, B. Investigation of nano-crystalline strontium hexaferrite magnet powder from mill-scale waste by the mechanochemical synthesis: Effect of the annealing temperature. *Mater. Chem. Phys.* **2022**, *290*, 126513. [CrossRef]
39. Choi, J.Y.; Lee, J.M.; Baek, Y.K.; Lee, J.G.; Kim, Y.K. Effect of sodium addition on structural and magnetic properties of solid state processed $SrFe_{12-x}Al_xO_{19}$ ($x \leq 4$). *Appl. Phys. A* **2022**, *128*, 1127. [CrossRef]
40. Sahoo, V.; Bhowmik, R.N.; Khan, S.A. Enhancement of electrical conductivity, optical band gap and ferromagnetic properties by co-doping of Co and Ti ions in canted antiferromagnetic hematite (α-Fe_2O_3) system. *Mater. Chem. Phys.* **2023**, *296*, 127298. [CrossRef]
41. Kumar, V.; Ahlawat, D.S.; Ul Islam, S.A.; Singh, A. Ce doping induced modifications in structural, electrical and magnetic behaviour of hematite nanoparticles. *Mater. Sci. Eng. B* **2021**, *272*, 115327. [CrossRef]

42. Dudziak, S.; Ruzynska, Z.; Bielan, Z.; Ryl, J.; Klimczuk, T.; Zielinska-Jurek, A. Pseudo-superparamagnetic behavior of barium hexaferrite particles. *RSC Adv.* **2020**, *10*, 18784. [CrossRef] [PubMed]
43. Shezad, M.; Liu, X.; Feng, S.; Kan, X.; Wang, W.; Liu, C.; Shehzad, T.J.; Rehman, K.M.U. Characterizations analysis of magneto-structural transitions in Ce-Co doped SrM based nano $Sr_{1-x}Ce_xFe_{12-x}Co_xO_{19}$hexaferrite crystallites prepared by ceramic route. *J. Magn. Magn. Mater.* **2020**, *497*, 166013. [CrossRef]
44. Turchenko, V.; Kostishin, V.G.; Trukhanov, S.; Damay, F.; Balasoiu, M.; Bozzo, B.; Fina, I.; Burkhovetsky, V.V.; Polosan, S.; Zdorovets, M.V.; et al. Structural features, magnetic, and ferroelectric properties of $SrFe_{10.8}In_{1.2}O_{19}$ compound. *Mater. Res. Bull.* **2021**, *138*, 111236. [CrossRef]
45. Xu, Y.F.; Ma, Y.Q.; Xu, S.T.; Zan, F.L.; Zheng, G.H.; Dai, Z.X. Effects of vacancy and exchange-coupling between grains on magnetic properties of $SrFe_{12}O_{19}$ and α-Fe_2O_3 composites. *Mater. Res. Bull.* **2014**, *57*, 13–18. [CrossRef]
46. Yasmin, N.; Iqbal, M.Z.; Zahid, M.; Gillani, S.F.; Ashiq, M.N.; Inam, I.; Abdulsatar, S.; Safdar, M.; Mirza, M. Structural and magnetic studies of Ce-Zn doped M-type $SrFe_{12}O_{19}$ hexagonal ferrite synthesized by sol-gel auto-combustion method. *Ceram. Int.* **2019**, *45*, 462–467. [CrossRef]
47. Tan, G.; Chen, X. Synthesis, structures and multiferroic properties of strontium hexaferrite ceramics. *J. Electr. Mater.* **2013**, *42*, 906–911. [CrossRef]
48. Atif, M.; Alvi, M.H.; Ulah, S.; Rehman, A.U.; Nadeem, M.; Khalid, W.; Ali, Z.; Guo, H. Impact of strontium substitution on the structural, magnetic, dielectric and ferroelectric properties of $Ba_{1-x}Sr_xFe_{11}Cr_1O_{19}$ (x = 0.0–0.8) hexaferrites. *J. Magn. Magn. Mater.* **2020**, *500*, 166414. [CrossRef]
49. Turchenko, V.; Bondyakov, A.S.; Trukhanov, S.; Fina, I.; Korovishkin, V.V.; Balasoiu, M.; Polosan, S.; Bozzo, B.; Lupu, N.; Trukhanov, A. Microscopic mechanism of ferroelectric properties in barium hexaferrites. *J. Alloys Compd.* **2023**, *931*, 167433. [CrossRef]
50. Bhat, B.H.; Samad, R.; Want, B. Dielectric and impedance behavior of neodymium substituted strontium hexaferrite. *Appl. Phys. A* **2016**, *122*, 810. [CrossRef]
51. Nikolic, M.V.; Lukovic, M.D.; Labus, N.J. Influence of humidity on complex impedance and dielectric properties of iron manganite ($FeMnO_3$). *J. Mater. Sci. Mater. Electron.* **2019**, *30*, 12399–12405. [CrossRef]
52. Bondarenko, A.S.; Ragoisha, G. EIS Spectrum Analyzer. Available online: https://www.abc.chemistry.bsu.by (accessed on 25 November 2016).
53. Nikolic, M.V.; Sekulic, D.L.; Vasiljevic, Z.Z.; Lukovic, M.D.; Pavlovic, V.B.; Aleksic, O.S. Dielectric properties, complex impedance and electrical conductivity of Fe_2TiO_5 nanopowder compacts and bulk samples at elevated temperatures. *J. Mater. Sci. Mater. Electron.* **2017**, *28*, 4796–4806. [CrossRef]
54. Anis-ur-Rehman, M.; Kanwal, S.; Khan, Z.; Asif, A.; Hussain, A.N.; Zahid, S. Study of dielectric relaxations in co precipitated Sr-Fe(Cr) nanoferrites. *J. Mater. Sci. Mater. Electron.* **2015**, *26*, 6539–6545. [CrossRef]
55. Aziz, A.; Ahmed, E.; Ali, I.; Athar, M.; Ehsan, M.F.; Ashiq, M.N. Effect of Gd and Cu on the structural, electrical, and dielectric properties of $MnFeO_3$ nanomaterials synthesized by the sol-gel method. *J. Electron. Mater.* **2015**, *44*, 4300–4307. [CrossRef]